CHINESE OPTICS LETTERS

Vol. 19, No. 9 | September 2021

Liquid crystal integrated metamaterial for multi-band terahertz linear polarization conversion

Shitong Xu (许士通)[1*], Fei Fan (范 飞)[2], Hongzhong Cao (曹洪忠)[1], Yinghua Wang (王英华)[1], and Shengjiang Chang (常胜江)[2,3]

[1] Shandong Provincial Key Laboratory of Laser Polarization and Information Technology, Department of Physics, School of Physics and Engineering, Qufu Normal University, Qufu 273165, China

[2] Institute of Modern Optics, Tianjin Key Laboratory of Micro-Scale Optical Information Science and Technology, Nankai University, Tianjin 300350, China

[3] Tianjin Key Laboratory of Optoelectronic Sensor and Sensing Network Technology, Tianjin 300350, China

*Corresponding author: xustonenk@163.com

Received January 26, 2021 | Accepted March 3, 2021 | Posted Online May 31, 2021

We experimentally investigate the linear polarization conversion for terahertz (THz) waves in liquid crystal (LC) integrated metamaterials, which consist of an LC layer sandwiched by two orthogonally arranged sub-wavelength metal gratings. A Fabry–Perot-like cavity is well constructed by the front and rear gratings, and it shows a strong local resonance mechanism, which greatly enhances the polarization conversion efficiency. Most importantly, the Fabry–Perot-like resonance can be actively tuned by modulating the refractive index of the middle LC layer under the external field. As a result, the integrated metamaterial achieves multi-band tunable linear polarization conversion.

Keywords: terahertz; liquid crystals; metamaterial; polarization conversion.
DOI: 10.3788/COL202119.093701

1. Introduction

With the continuous progress of terahertz (THz) sources and detection technology, THz science has made great progress[1], and it has shown great application prospects in wireless communication[2], spectral detection[3], and human security[4]. To realize these applications, functional devices such as THz modulators[5], waveguides[6], switches[7], isolators[8], and polarization devices[9–12] are essential. In particular, polarization conversion devices play an important role in polarization imaging and polarized light communications[13]. However, the existing polarization devices in THz bands mainly rely on natural birefringent crystals[14] and sub-wavelength metal gratings, which cannot achieve active regulation once the structural parameters are determined. Therefore, it is urgent to study functional materials with microstructures for active THz devices.

Based on the larger birefringence and low loss of liquid crystal (LC) in the THz band, as well as the controllable refractive index of the outfield, LCs can be used as tunable functional materials to realize the flexible control of the amplitude, phase, and polarization of THz waves[15–17]. However, for the independent LC layer, the thickness generally needs to be in the sub-millimeter range to meet the phase accumulation that is required by a 1/4 or 1/2 wave-plate in the THz band. Consequently, the thick LC layer results in a series of problems such as poor pre-alignment and needs a larger drive outfield[18,19]. For instance, Hsieh *et al.* reported an electrically controlled 1/4 wave-plate in the THz band, which achieved the $\pi/2$ phase shift in the 570-μm-thick E7-LC at a high voltage of 125 V[20]. Besides, the lack of a transparency electrode further restricts the development of THz LC devices[21,22].

Recently, an LC integrated metamaterial has attracted great attention for its superiority in phase and polarization control, which can not only realize the active tuning in compact structures but also improve the device performance and reduce the driving field[23–27]. For example, Vasić *et al.* reported an LC-infiltrated metal-insulator-metal metamaterial, which realizes the electrically tunable THz polarization conversion under the lower driving voltage[28]. In addition to achieving polarization control, the metamaterial itself can also be used for THz LC electrodes[29]. However, the LC orientation technology of the rubbing alignment or photo-alignment can make the LC layer well aligned within ~100 μm, but it is difficult to orient the intermediate layer when the LC layer is thick[30]. Therefore, the thicker LC cell may result in the problems of a larger drive outfield and a limited modulation range of THz LC devices.

Here, we propose an LC integrated metal grating (LCMG), which achieves multi-band polarization conversion in the transmission mode. In the pre-orientation of the TM field, the LC molecules can well be oriented or revert to the anchoring state by the variable electric (E) field through the metal grating

electrode. Depending on the local resonance, not merely the LC birefringence, the polarization conversion efficiency of the LCMG is greatly enhanced. Moreover, the unidirectional transmissions are realized, resulting from the 90° linear polarization transformation, which has a high extinction ratio exceeding 20 dB at the resonance frequency.

2. Experimental Methods

Figure 1 shows the structure of the proposed LCMG, and it is mainly a cell composed of two orthogonally arranged sub-wavelength metal gratings filled with 4-cyano-4'-pentylbiphenyl (5CB) LC of 500 μm thickness. The metal gratings are fabricated by conventional photolithography with the 200-nm-thick gold layer on a 500-μm-thick silica substrate[31]. Here, an E-field and a magnetic field (M-field) were applied to manipulate the LC molecules. A set of permanent magnets provided a static M-field of 0.17 T to pre-anchor the LC molecules along the x axis. The metal gratings that are connected on one side are used as the front and rear electrodes. A variable E-field can be applied when the bias field is applied on these two metal gratings. Here, the E-field intensity of 1 kV/m corresponds to a biased voltage of 0.5 V. Here, the 0.17 T M-field is large enough to make LC molecules uniformly oriented, which is coupled with a maximum E-field of 20 kV/m to regulate the LC layer[7]. The principle of LC orientation is as follows: at the beginning, as shown in Fig. 1(a), the LC molecules are arranged along the x axis under the force of a large M-field when the applied E-field is less than the threshold value ($E < 6\,\mathrm{kV/m}$). With the increase of the intensity of the applied E-field ($6\,\mathrm{kV/m} < E < 20\,\mathrm{kV/m}$), the LC molecules are in an intermediate state and begin to rotate towards the z axis under the combined action of E- and M-fields, as shown in Fig. 1(b). The LC molecules are mainly bound in the direction of the E-field when the applied E-field intensity exceeds 20 kV/m, as shown in Fig. 1(c). Therefore, the orientation of LC molecules can be freely controlled in the x–z plane by the combination of the E- and M- fields.

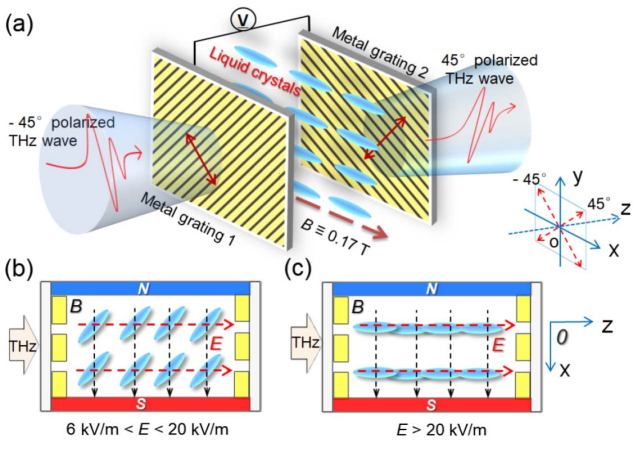

Fig. 1. Structure diagram of the liquid crystal integrated metal grating (LCMG) under the constant M-field and variable E-field ($B \| x$, $E \| z$); the coordinate axis is attached to the right. The diagram of LC orientation in the LCMG when (a) $E < 6$ kV/m; (b) 6 kV/m $< E <$ 20 kV/m; (c) $E >$ 20 kV/m.

The experiment was carried out through the self-built THz time-domain spectroscopy (THz-TDS) system[32] shown in Fig. 2(a). Here, the THz pulse was generated by a low-temperature grown GaAs photo-conductive antenna (PCA), and a (110) ZnTe crystal was used for detection. The excitation source was a Ti:sapphire laser with a central wavelength of 800 nm and a 75 fs duration with an 80 MHz repetition rate. Besides, the NdFeB permanent magnets are placed in a three-dimensional (3D)-printed mold to apply a TM field, and the longitudinal E-field is applied by wires that are connected to the front and rear metal gratings. The sample is vertically fixed to the hollow aluminum test platform with a pore diameter of 1 cm.

In Fig. 2(b), the birefringence characteristic of the discrete 5CB LC was investigated by THz-TDS. Here, LCs were filled between two layers of quartz plates, in which the inner surfaces were covered with the graphite electrode[7]. A longitudinal E-field is applied by connecting the wire to the graphite electrode, and the TM field of 0.17 T always exists. The THz wave emitted from the PCA into the sample is vertically polarized. Therefore, the 90° and 0° orientations of the LC with the input polarized light can be achieved by changing the E-field strength, which correspond to 0 kV/m and 20 kV/m, respectively. In Fig. 2(b), the time-domain spectra of 0° orientation lags significantly behind that of 90° orientation, which means it has a larger refractive index. The refractive index of the LC can be obtained through the Fourier transform of the time-domain signal. From Fig. 2(c), we find that the 5CB LC has little dispersion in the testing band, the refractive indexes of e and o light are about $n_e = 1.65$ and $n_o = 1.55$, respectively, and the birefringence is 0.1. Besides, the polarizing property of the sub-wavelength metal grating is experimentally and simulatively investigated, as

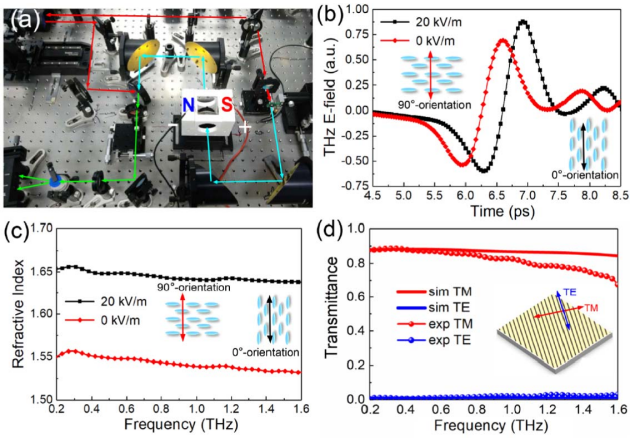

Fig. 2. (a) Experimental light path of the THz-TDS system; the sample is placed in a 3D-printed mold with a set of permanent magnets, and the E-field is applied by the connected wires. The experimentally measured (b) time-domain signals and (c) refractive index of the LC with 90° and 0° orientations under the E-field of 0 and 20 kV/m. (d) The experimental and simulative transmission of the metal grating at TM and TE polarization modes.

shown in Fig. 2(d). Here, the grating period is 20 μm, while the wire width is 14 μm. TM and TE modes, respectively, indicate that the polarization direction of the incident light is parallel and perpendicular to the orientation of the metal wire. We can find that the THz waves have a high transmittance in the TM mode, while it is almost totally reflected in the TE mode; therefore, this sub-wavelength metal grating can be seen as a high-efficiency THz polarizer.

3. Results and Discussions

Next, we will discuss the polarization conversion characteristics of the composite devices (LCMG). As mentioned above, the directions of the front and back grating layers are both arranged with an angle of 45° to the x axis. When the external E-field is small ($E < 6\,\mathrm{kV/m}$), the optical axis of the LC will be arranged along the x axis under the larger M-field. Therefore, the linear polarization of the incident light passes through metal grating 1 forming an angle of 45° with the optical axis of the LC. According to the knowledge of polarization optics, the incident linear polarization will be converted into circular polarization, elliptical polarization, or orthogonal linear polarization based on the LC polarization conversion. Due to the existence of metal grating 2 as an analyzer, only the 45° polarized THz waves can be output from the LCMG. However, the effective birefringence coefficient of the LC layer will gradually decrease, and its polarization conversion ability will be weakened when the LC orientation is in the intermediate state ($6\,\mathrm{kV/m} < E < 20\,\mathrm{kV/m}$). Lastly, the LC molecules will eventually be aligned strictly along the z axis when the E-field is greater than 20 kV/m.

The results in polarization conversion of the LCMG with different E-fields are shown in Fig. 3. The THz time-domain signals

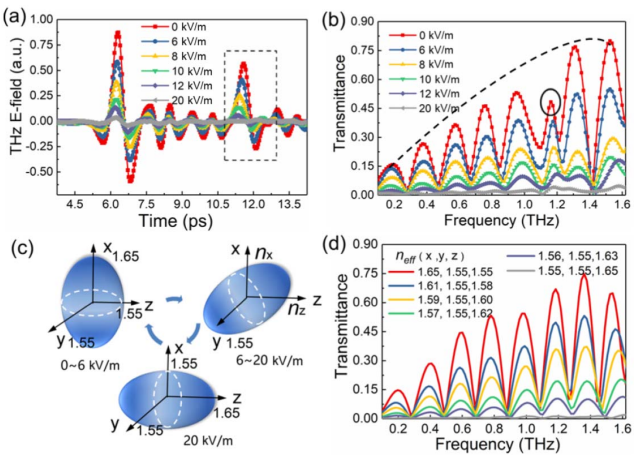

Fig. 3. Experimental (a) time-domain signals and (b) transmission spectra of the LCMG when the E-fields increase from 0 to 20 kV/m. (c) The diagrams of the effective refractive index (n_{eff}) ellipsoids of the LC with the E-field at 0–6 kV/m, 6–20 kV/m, and 20 kV/m. (d) The simulated transmittance spectra when the LC molecules are orientated with different angles to the coordinate axis.

of the LCMG shown in Fig. 3(a) can be divided into two parts: the first part is the main cycle pulse starting from 4.5 to 7.5 ps with several low-amplitude oscillations from 7.5 to 10.5 ps; the second part is a deputy pulse from 10.5 to 13 ps. As the E-field intensity increases from 0 kV/m to 20 kV/m, the peak value of the time-domain signal linearly decreases. The main pulse has no phase change, while the deputy pulse has a slight forward change as the E-field increases. Figure 3(b) shows transmittance spectra from the Fourier transform, and it has many periodic resonance peaks (i.e., 0.17 THz, 0.37 THz, 0.57 THz . . .) and valleys (i.e., 0.27 THz, 0.47 THz, 0.67 THz . . .) with the fixed frequency intervals of 0.2 THz from 0.1 THz to 1.6 THz. These frequencies satisfy the Fabry–Perot resonance condition, which follows[33]:

$$\Delta\nu = c/2n_{\mathrm{eff}}h. \tag{1}$$

Here, c is the speed of light in vacuum, h is the thickness of the LC layer, and n_{eff} is the equivalent refractive index of the LC in the Fabry–Perot cavity. In the rotation process of the LC molecules from the x axis to the z axis, the equivalent refractive index gradually approaches n_o, and it finally equals n_o when LC molecules are aligned strictly along the z axis. This just explains the slight phase shift of the deputy pulse in Fig. 3(a). Here, we simplify $n_{\mathrm{eff}} = n_o = 1.55$ to facilitate discussion. Then we can get that $\Delta\nu$ is approximately equal to 0.2 THz. It is worth noting that: 1) the transmittance spectral peaks have a spectral envelope shown in the dotted line in Fig. 3(b), which is similar to the frequency selection effect of non-monochromatic light incident into the Fabry–Perot cavity; 2) based on the multiple reflections in the metal Fabry–Perot-like cavity, several transmittance peaks are attributed to the contribution of the deputy pulse; 3) according to Eq. (1), the frequency interval $\Delta\nu$ of the spectral lines can be modulated by changing the thickness of the LC layer; 4) due to the presence of water absorption in the THz wave, the above law is not well matched at the resonance peaks of 1.16 THz; 5) with the increase of the E-field, the transmittances of peaks gradually decline, and the resonance position does not change with the outfield.

In order to verify the authenticity of the experiment, we performed a simulation of LCMG by using CST software[34]. We set two pairs of periodic boundary conditions, which are perpendicular to the transmission direction. We use the plane wave to stimulate and a probe to detect. Based on the experimental test data, the material with a dielectric constant of 3.61 was used to represent silica, and the metal gratings are set to be gold. To reflect the orientation change of the optical axis of the LC under the external field, we use the refractive index ellipsoid to simulate the LC molecule, where n_x, n_y, and n_z represent the effective refractive index of the LC at the x, y, and z axes, respectively, as shown in Fig. 3(c). In this work, n_y remains a constant of $n_o = 1.55$, n_x decreases, and n_z increases during the rotation of the LC optical axis from x to the z axis. Therefore, the corresponding refractive index ellipsoid can be expressed as $n_{x,y,z}$ (1.65, 1. 55, 1.55) and $n_{x,y,z}$ (1.55, 1.55, 1.65) in the case of LC molecules that are arranged along the

x and z axes. The LC refractive index ellipsoid in the intermediate state can be calculated by[35]

$$\begin{aligned} n_y &= n_o, \\ n_x(\theta) &= n_o n_e / \sqrt{n_o^2 \cos^2\theta + n_e^2 \sin^2\theta}, \\ n_z(\theta) &= n_o n_e / \sqrt{n_o^2 \sin^2\theta + n_e^2 \cos^2\theta}. \end{aligned} \tag{2}$$

Here, the orientation angle θ indicates the long axis of the LC with the x coordinate axis. The detailed parameters of the simulated LC refractive index ellipsoid with different orientation angle θ and external E-field are listed in Table 1. In this way, we have obtained the simulated transmittance spectrum, as shown in Fig. 3(d), which is consistent with the experimental results.

The diagram of THz wave transmission and polarization evolution in the LCMG is illustrated in Fig. 4. Here, the Fabry–Perot-like cavity is well constructed by the polarizer and analyzer of the metal gratings. Firstly, the vertically polarized light incident into metal grating 1 will be converted into a −45° linear polarization. As shown in Fig. 4(a), the LC layer is arranged along the x axis under the action of a magnet when $E < 6\,\mathrm{kV/m}$. Due to the LC layer acting as a polarization wave-plate, the −45° linear polarization is mostly converted into the elliptical polarization. The part of the elliptical polarization state that is perpendicular to metal grating 2 can be directly output from the device, but the remaining will reflect into the Fabry–Perot-like cavity and form the local resonance. In every reflection period, the new 45° linearly polarized component will be produced. However, the LC layer cannot achieve polarization conversion when the LC is oriented along the z axis ($E > 20\,\mathrm{kV/m}$), and then no light can be output from the device, as shown in Fig. 4(b). Besides, the resonance peaks are linearly decreased when $6\,\mathrm{kV/m} < E < 20\,\mathrm{kV/m}$, which well explains the experimental results in Fig. 3(b). Therefore, the higher modulation depth of the tunable polarization conversion in the LCMG originates from the local resonance and the multiple polarization section in the Fabry–Perot-like cavity, not merely the refractive index change of the LC.

Table 1. Detailed Parameters of Simulated LC Refractive Index Ellipsoid with Different Orientation Angles θ and External E-Field.

E-Field Experiments	0 V	6 V	8 V	10 V	12 V	20 V
θ (fitted)	0°	35°	48°	60°	70°	90°
n_{eff} ($n_{x,y,z}$) (simulated)	1.65,	1.61,	1.59,	1.57,	1.56,	1.55,
	1.55,	1.55,	1.55,	1.55,	1.55,	1.55,
	1.55	1.58	1.60	1.62	1.63	1.65

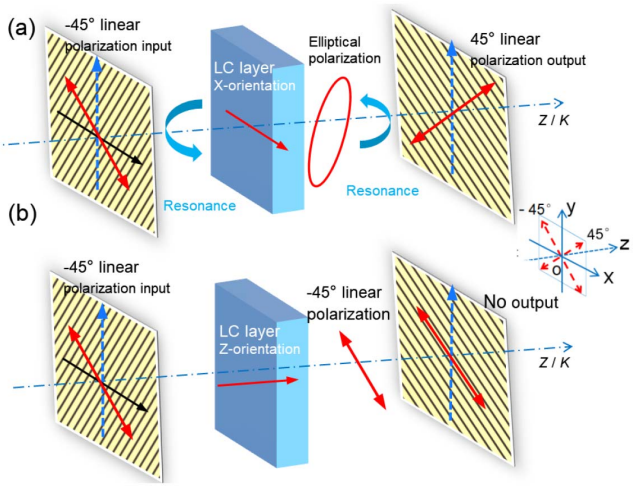

Fig. 4. Polarization evolution in the LCMG when the LC layer is in the (a) x and (b) z orientations.

Besides, we present the E-vector distribution of the LCMG at 0.78 THz (resonance peaks) under different LC orientation. Figures 5(a)–5(c) show the E-vector distribution of the LCMG at the x–y cutting view with a different plane when $0 < E < 6\,\mathrm{kV/m}$. The orientation of the E-vector just reflects the direction of the THz polarization state. The input plane that passed through metal grating 1 with a −45° polarization state is shown in Fig. 5(a). The E-vector is rotating anticlockwise in the middle plane of the LC layer, which changes to be an elliptically polarized light, as shown in Fig. 5(b). Figure 5(c) shows that the E-vector turns into 45° polarization at the output plane after passing through metal grating 2. Furthermore, we compared the E-vector distributions in the y–z cutting plane of the LCMG when the LC was oriented along the x and z axes, as shown in Figs. 5(d) and 5(e). It can be seen that the E-field presents periodic resonance distribution within the LC layer, which is confined between the front and rear metal gratings. A large proportion of THz waves can be output from the grating 2 in Fig. 5(d), while it is forbidden in Fig. 5(e). Here, the direction

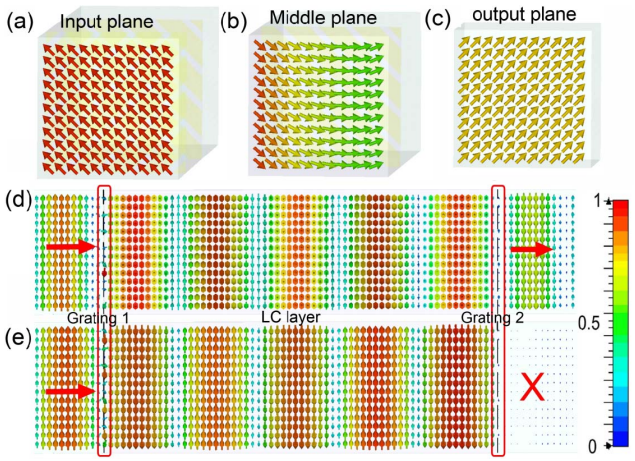

Fig. 5. Distribution of the E-vector at the (a) input plane, (b) middle plane, and (c) output plane of the x–y cutting view in the LCMG when the LC layer is in the x orientation at 0.78 THz. The arrows indicate the direction of the THz polarization. The y–z cutting plane of E-vector distributions in the LCMG when the LC layer is in the (d) x orientation or (e) z orientation.

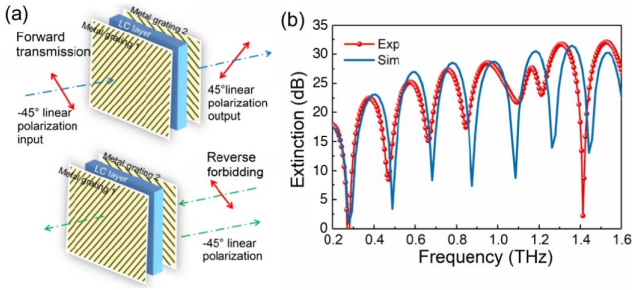

Fig. 6. (a) Working principle diagram of the unidirectional transmission in the LCMG. (b) The extinction ratios of unidirectional transmission; the experimental and simulated data are represented by the dotted line and straight line, respectively.

and magnitude of the *E*-vector directly reflect the polarization conversion and internal resonance mechanism discussed in Fig. 4.

Based on the 90° linear polarization conversion of the device, unidirectional transmission can be realized when we incident the same linearly polarized light from back and forth (here the polarization orientation is parallel or perpendicular to the directions of the metal grating). For example, if a −45° linear polarization light is incident from metal grating 1 into the LCMG, we can obtain the 45° polarized wave and its transmittance curve, as shown in the red line in Fig. 3(b). But, for the same linear polarization of −45°, polarized light incident from the opposite direction is prohibited, as shown in Fig. 6(a). We can use the extinction ratio to characterize the unidirectional transmission performance, which follows[36]:

$$\mathrm{Ext} = 20\ \log[t_{\mathrm{forward}}/t_{\mathrm{backward}}]. \tag{3}$$

Here, t_{forward} and t_{backward} are the transmittance of the LCMG from forward and backward, respectively. It can be seen from the Fig. 6(b) that the extinction ratio of the device is greater than 20 dB at the resonant frequency. The difference in the deep valley at 1.41 THz between the experiments and simulation may come from the water absorption and mechanical vibration of the platform in the experiment.

4. Conclusions

An LC integrated metamaterial composed of two metal gratings infiltrated with an LC layer was proposed. Here, the metal gratings play multiple roles: 1) transparent electrode of the LC layer; 2) THz polarizer to control the polarization; 3) construct the Fabry–Perot-like cavity. A local resonance mechanism in the integrated metamaterial has been experimentally and numerically presented, and it is confirmed that this mechanism is not merely contributed by the birefringence of the LC, but also the resonance in the micro-cavity. As a result, active linear polarization conversion and unidirectional transmission were realized at the multi-band. Besides, the frequency interval of Fabry–Perot-like resonance can be adjusted by changing the thickness of the LC layer. We believe this LC integrated metamaterial for THz polarization control will bring new ideas for the development and application of THz LC devices.

Acknowledgement

This work was supported by the National Natural Science Foundation of China (Nos. 62005143, 61831012, and 61971242), the Natural Science Foundation of Tianjin (No. 19JCYBJC16600), and the Young Elite Scientists Sponsorship Program by Tianjin (No. TJSQNTJ-2017-12).

References

1. X.-C. Zhang, A. Shkurinov, and Y. Zhang, "Extreme terahertz science," Nat. Photon. **11**, 16 (2017).
2. A. S. Cacciapuoti, K. Sankhe, M. Caleffi, and K. R. Chowdhury, "Beyond 5G: THz-based medium access protocol for mobile heterogeneous networks," IEEE Commun. Mag. **56**, 110 (2018).
3. X. Yang, X. Zhao, K. Yang, Y. Liu, Y. Liu, W. Fu, and Y. Luo, "Biomedical applications of terahertz spectroscopy and imaging," Trends Biotechnol. **34**, 810 (2016).
4. J. F. Federici, B. Schulkin, F. Huang, D. Gary, R. Barat, F. Oliveira, and D. Zimdars, "THz imaging and sensing for security applications—explosives, weapons and drugs," Semicond. Sci. Tech. **20**, s266 (2005).
5. S. Chen, F. Fan, Y. Miao, X. He, K. Zhang, and S. Chang, "Ultrasensitive terahertz modulation by silicon-grown MoS_2 nanosheets," Nanoscale **8**, 4713 (2016).
6. H. Pahlevaninezhad, B. Heshmat, and T. Darcie, "Advances in terahertz waveguides and sources," IEEE Photon. J. **3**, 307 (2011).
7. S.-T. Xu, F. Fan, Y.-Y. Ji, J.-R. Cheng, and S.-J. Chang, "Terahertz resonance switch induced by the polarization conversion of liquid crystal in compound metasurface," Opt. Lett. **44**, 2450 (2019).
8. M. Shalaby, M. Peccianti, Y. Ozturk, and R. Morandotti, "A magnetic non-reciprocal isolator for broadband terahertz operation," Nat. Commun. **4**, 1558 (2013).
9. J. Zi, Q. Xu, Q. Wang, C. Tian, Y. Li, X. Zhang, J. Han, and W. Zhang, "Antireflection-assisted all-dielectric terahertz metamaterial polarization converter," Appl. Phys. Lett. **113**, 101104 (2018).
10. X. Luo, Z. Tan, C. Wang, and J. Cao, "A reflecting-type highly efficient terahertz cross-polarization converter based on metamaterials," Chin. Opt. Lett. **17**, 093101 (2019).
11. H.-F. Zhang, L. Zeng, G.-B. Liu, and T. Huang, "Tunable linear-to-circular polarization converter using the graphene transmissive metasurface," IEEE Access **7**, 158634 (2019).
12. H.-F. Zhang, H. Zhang, Y. Yao, J. Yang, and J.-X. Liu, "A band enhanced plasma metamaterial absorber based on triangular ring-shaped resonators," IEEE Photon. J. **10**, 5700610 (2018).
13. T. Nagatsuma, G. Ducournau, and C. C. Renaud, "Advances in terahertz communications accelerated by photonics," Nat. Photon. **10**, 371 (2016).
14. J.-B. Masson and G. Gallot, "Terahertz achromatic quarter-wave plate," Opt. Lett. **31**, 265 (2006).
15. D. Andrienko, "Introduction to liquid crystals," J. Mol. Liq. **267**, 520 (2018).
16. L. Wang, X.-W. Lin, X. Liang, J.-B. Wu, W. Hu, Z.-G. Zheng, B.-B. Jin, Y.-Q. Qin, and Y.-Q. Lu, "Large birefringence liquid crystal material in terahertz range," Opt. Mater. Express **2**, 1314 (2012).
17. Y. Shen, Z. Shen, G. Zhao, and W. Hu, "Photopatterned liquid crystal mediated terahertz Bessel vortex beam generator," Chin. Opt. Lett. **18**, 080003 (2020).
18. Y. Ji, F. Fan, S. Xu, J. Yu, and S. Chang, "Manipulation enhancement of terahertz liquid crystal phase shifter magnetically induced by ferromagnetic nanoparticles," Nanoscale **11**, 4933 (2019).
19. L. Yang, F. Fan, M. Chen, X. Zhang, J. Bai, and S. Chang, "Magnetically induced birefringence of randomly aligned liquid crystals in the terahertz regime under a weak magnetic field," Opt. Mater. Express **6**, 2803 (2016).

20. C.-F. Hsieh, R.-P. Pan, T.-T. Tang, H.-L. Chen, and C.-L. Pan, "Voltage-controlled liquid-crystal terahertz phase shifter and quarter-wave plate," Opt. Lett. **31**, 1112 (2006).
21. C.-S. Yang, T.-T. Tang, P.-H. Chen, R.-P. Pan, P. Yu, and C.-L. Pan, "Voltage-controlled liquid-crystal terahertz phase shifter with indium-tin-oxide nano-whiskers as transparent electrodes," Opt. Lett. **39**, 2511 (2014).
22. Y. Wu, X. Ruan, C.-H. Chen, Y. J. Shin, Y. Lee, J. Niu, J. Liu, Y. Chen, K.-L. Yang, and X. Zhang, "Graphene/liquid crystal based terahertz phase shifters," Opt. Express **21**, 21395 (2013).
23. Z. Shen, S. Zhou, S. Ge, W. Duan, P. Chen, L. Wang, W. Hu, and Y. Lu, "Liquid-crystal-integrated metadevice: towards active multifunctional terahertz wave manipulations," Opt. Lett. **43**, 4695 (2018).
24. Z.-X. Shen, S.-H. Zhou, S.-J. Ge, W. Hu, and Y.-Q. Lu, "Liquid crystal enabled dynamic cloaking of terahertz Fano resonators," Appl. Phys. Lett. **114**, 041106 (2019).
25. Z. Shen, S. Zhou, X. Li, S. Ge, P. Chen, W. Hu, and Y.-Q. Lu, "Liquid crystal integrated metalens with tunable chromatic aberration," Adv. Photon. **2**, 036002 (2020).
26. G. Isić, B. Vasić, D. C. Zografopoulos, R. Beccherelli, and R. Gajić, "Electrically tunable critically coupled terahertz metamaterial absorber based on nematic liquid crystals," Phys. Rev. Appl. **3**, 064007 (2015).
27. Z.-X. Shen, M.-J. Tang, P. Chen, S.-H. Zhou, S.-J. Ge, W. Duan, T. Wei, X. Liang, W. Hu, and Y.-Q. Lu, "Planar terahertz photonics mediated by liquid crystal polymers," Adv. Opt. Mater. **8**, 1902124 (2020).
28. B. Vasić, D. C. Zografopoulos, G. Isić, R. Beccherelli, and R. Gajić, "Electrically tunable terahertz polarization converter based on overcoupled metal-isolator-metal metamaterials infiltrated with liquid crystals," Nanotechnology **28**, 124002 (2017).
29. L. Wang, S. Ge, W. Hu, M. Nakajima, and Y. Lu, "Tunable reflective liquid crystal terahertz waveplates," Opt. Mater. Express **7**, 2023 (2017).
30. L. Wang, X.-W. Lin, W. Hu, G.-H. Shao, P. Chen, L.-J. Liang, B.-B. Jin, P.-H. Wu, H. Qian, and Y.-N. Lu, "Broadband tunable liquid crystal terahertz waveplates driven with porous graphene electrodes," Light-Sci. Appl. **4**, e253 (2015).
31. S.-T. Xu, F. Fan, M. Chen, Y.-Y. Ji, and S.-J. Chang, "Terahertz polarization mode conversion in compound metasurface," Appl. Phys. Lett. **111**, 031107 (2017).
32. Y.-Y. Ji, F. Fan, S.-T. Xu, J.-P. Yu, Y. Liu, X.-H. Wang, and S.-J. Chang, "Terahertz dielectric anisotropy enhancement in dual-frequency liquid crystal induced by carbon nanotubes," Carbon **152**, 865 (2019).
33. F. Fan, S.-T. Xu, X.-H. Wang, and S.-J. Chang, "Terahertz polarization converter and one-way transmission based on double-layer magneto-plasmonics of magnetized InSb," Opt. Express **24**, 26431 (2016).
34. X. Zhang, F. Fan, C.-Y. Zhang, Y.-Y. Ji, X.-H. Wang, and S.-J. Chang, "Tunable terahertz phase shifter based on dielectric artificial birefringence grating filled with polymer dispersed liquid crystal," Opt. Mater. Express **10**, 282 (2020).
35. I. Khoo, D. H. Werner, X. Liang, A. Diaz, and B. Weiner, "Nanosphere dispersed liquid crystals for tunable negative-zero-positive index of refraction in the optical and terahertz regimes," Opt. Lett. **31**, 2592 (2006).
36. S.-T. Xu, F. T. Hu, M. Chen, F. Fan, and S. J. Chang, "Broadband terahertz polarization converter and asymmetric transmission based on coupled dielectric-metal grating," Ann. Phys-Berlin **529**, 1700151 (2017).